Supplementary Information

Individualized defocusing particle tracking for dynamic surface profilometry

Sean MacKenzie, Alexander Eden, David Huber, Sumita Pennathur

Department of Mechanical Engineering, University of California Santa Barbara,
Santa Barbara, California 93106, United States
E-Mail: sean_mackenzie@ucsb.edu

INDEX

Supplementary movie captions

References

Table S1. Assumptions for design rationale of IDPT algorithm

Qualitative description	Expression	Physical reason
A particle's in-plane displacement (Δx_i) will be much less than its out-of-plane displacement (Δz_i).	$\Delta x_i \ll \Delta z_i$	Geometry: out-of-plane stiffness vs. in-plane stiffness
The difference between two particles' out-of-plane positions (Δz_{ij}) will be much less than the in-plane distance between them (Δx_{ij}).	$\Delta z_{ij} \ll \Delta x_{ij}$	Smooth surface, small surface curvature
A particle's in-plane position for all times ($x_i(t)$) will be within a small local vicinity ($\pm \Delta x_i$) of its initial position (x_i^o).	$x_i(t) = x_i^o \pm \Delta x_i$	In-plane stiffness, no hysteresis
The in-plane position of a particle at-rest ($x_i(\Delta z_i = 0)$) will be the same for all times ($x_i(t, \Delta z_i = 0)$).	$x_i(t, \Delta z_i = 0) = x_i(\Delta z_i = 0)$	No hysteresis

Table S2. List of symbols and parameters

Symbol	Description

a — Radius of disc.

c — Similarity value.
$c(u, v)$ — 2D similarity map.
$c(u, v, z)$ — Stack of 2D similarity maps.

c_m — Maximum similarity value, or similarity.
$\overline{c_m}(z)$ — Local mean similarity at depth position z.
$\overline{c_m}$ — Depth-averaged mean similarity: the average of $\overline{c_m}(z)$ over all z positions.

$\Delta_c z$ — Axial step size between calibration images.

$\varepsilon_{z,i}$ — Measured particle error, depth coordinate.

f — Function that maps target particles to calibration particles.

h — Axial measurement range.

i — Target particle identification number.
k — Calibration particle identification number.

I — Image.

I_c — Calibration image.
$I_c(z)$ — Calibration image collection.
$I_c(z^o)$ — Calibration baseline image.

I_c^k — Calibration particle sub-image.
$I_c^k(z)$ — Calibration particle sub-image stack, or calibration stack.

I_t — Evaluation image.
$I_t(t)$ — Test image collection.
$I_t(t^o)$ — Test baseline image.

I_t^i — Target particle sub-image.
$I_t^i(t)$ — Target particle sub-image stack, or target particle stack.

Symbol	Description
L_c	Size of calibration particle sub-image.
L_t	Size of target particle sub-image.
N_{cal}	Number of calibration images.
N_{test}	Number of evaluation images.
N_p	Number of measurable particles per image.
N_p'	Number of measured particles per image.
N_p'/N_p	Relative number of measured particles per image.
N_p''	Number of identified particles per image.
$\overline{N_p'}$	Global mean number of measured particles per image.
$\overline{N_p'}(z)$	Local mean number of measured particles per image at depth position z.
$\overline{N_p'}(z)/N_p$	Local relative number of measured particles at depth position z.
$\overline{N_p'/N_p}$	Global mean relative number of measured particles.
r	Radial coordinate, physical space.
r_i'	Measured position, radial coordinate.
r^δ	Radial bin.
S	Similarity function.
$S\left(I_t^i, I_c^k(z)\right)$	Comparison of target particle sub-image against calibration stack via similarity function S.
$\sigma_{xy}(z)$	Local in-plane measurement uncertainty at depth position z.
$\overline{\sigma_{xy}}$	Depth-averaged in-plane uncertainty: the average of $\sigma_{xy}(z)$ over all z positions.
$\sigma_z(z)$	Local axial (depth) measurement uncertainty at depth position z.
$\overline{\sigma_z}$	Depth-averaged axial uncertainty: the average of $\sigma_z(z)$ over all z positions.
$\sigma_z^\delta(z)$	Local axial measurement uncertainty at depth position z for radial bin r^δ.
t	Time coordinate corresponding to images in test image collection.
t^o	Time point corresponding to the test baseline image.
u, v	In-plane coordinates, correlation space.
u^*, v^*, z^*	Position of maximum similarity value c_m in $c(u, v, z)$.
w	Surface displacement coordinate, out-of-plane direction.
$w(r)$	Surface displacement profile.
w_o	Peak deflection, $w(r = 0)$.
x, y, z	Coordinates in physical space.
x_i, y_i, z_i	Particle coordinates.
x_i', y_i', z_i'	Measured particle coordinates.
X, Y	Coordinates in image space.
X^o, Y^o	Baseline position, in-plane.
X_i^o, Y_i^o	Target particle baseline position.
X_k^o, Y_k^o	Calibration particle baseline position.

Symbol	Description
z	Axial coordinate along optical axis; depth position.
z_f	Axial position of the focal plane ($z_f = z = 0$).
z^o	Depth position corresponding to the calibration baseline image.
z^-, z^+	Lower and upper bounds of axial measurement range.

Note S3. Synthetic particle image generator settings

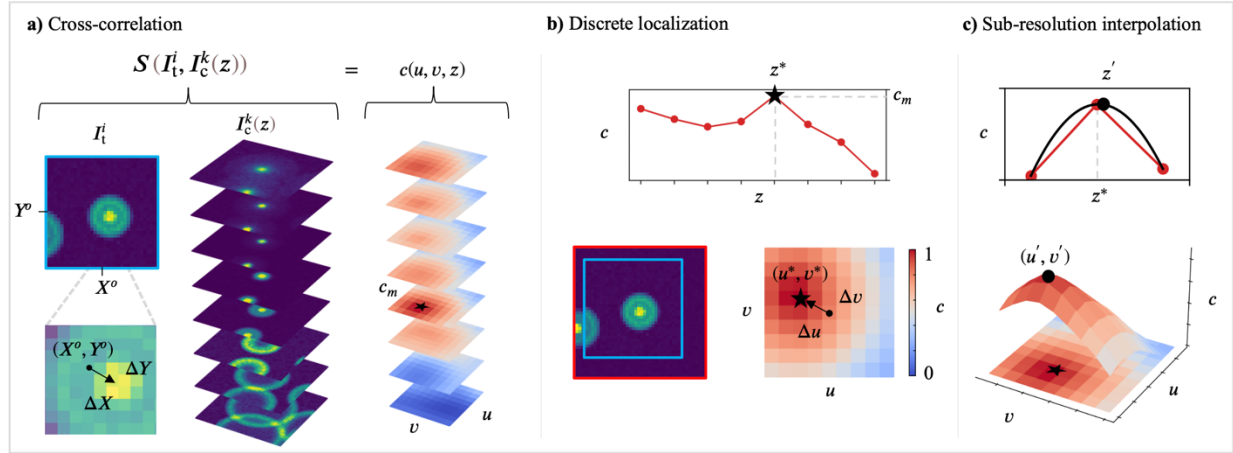|	
magnification:	10
numerical_aperture:	0.3
focal_length:	150
ri_medium:	1
ri_lens:	1.5
pixel_size:	4
pixel_dim_x:	256
pixel_dim_y:	256
background_mean:	100
points_per_pixel:	20
n_rays:	1000
gain:	1
cyl_focal_length:	0
particle_diameter:	1.0
background_noise:	5

Figure S4. Cross-correlation-based localization and sub-resolution interpolation. (a) Cross-correlation: A similarity function S compares a target particle sub-image I_t^i against each sub-image in its assigned calibration stack, $S\left(I_t^i, I_c^k(z)\right)$, resulting in a stack of 2D similarity maps $c(u, v, z)$. The position of maximum similarity, $c_m = c(u^*, v^*, z^*)$, is indicated by a black star. Bottom left: Close-up image of I_t^i showing the particle image shifted off-center by $(\Delta X, \Delta Y)$ relative to $I_t^i(X^o, Y^o)$. (b) Discrete localization: Top: Plot showing the maximum value from each 2D similarity map, $c(u^*, v^*)(z)$. Bottom left: Overlay of target particle template I_t^i (outlined in blue) and calibration template $I_c^k(z^*)$ (outlined in red) corresponding to the position of c_m. Bottom right: 2D similarity map $c(u, v, z^*)$, showing particle image shift $(\Delta X, \Delta Y)$ from (a) recorded as an equal and opposite shift in correlation space $(\Delta u, \Delta v)$, where $\Delta X = \Delta u$ and $\Delta Y = \Delta v$. (c) Sub-resolution interpolation: Top: Plot showing a parabolic three-point estimator fitted to $c(u^*, v^*)(z)$ centered on z^* to determine depth position z_i' with sub-calibration-sampling resolution. Bottom: 3D plot showing a 2D Gaussian function fitted to $c(u, v, z^*)$ to determine in-plane position (u_i', v_i') in correlation space, corresponding to in-plane position (x_i', y_i') in physical space. The synthetic particle images in (a-b) were generated using MicroSIG [1], using the settings given in note S3.

Table S5. Outlier qualifications from focal plane bias errors

Known depth position (z_i)	Measured depth position (z_i')	Focal plane bias error	Outlier
$z_i < -5$ μm	$z_i' < 0$	No	No
$z_i < -5$ μm	$z_i' > 0$	Yes	Yes
-5 μm $< z_i < 0$	$0 < z_i' < 5$ μm	Yes	Yes, if $\left\|\varepsilon_{z,i}\right\| > 5$ μm
$0 < z_i < 5$ μm	-5 μm $< z_i' < 0$	Yes	Yes, if $\left\|\varepsilon_{z,i}\right\| > 5$ μm
$z_i > 5$ μm	$z_i' < 0$	Yes	Yes
$z_i > 5$ μm	$z_i' > 0$	No	No

$\varepsilon_{z,i}$: depth measurement error

Table S6. Outliers by type for IDPT and GDPT

	Counts		Percent of Number Measured		Percent of True Number		Percent of Number Outliers	
	IDPT	GDPT	IDPT	GDPT	IDPT	GDPT	IDPT	GDPT
cmin	0	202	0	6.3	0	3.6	0.0	16.4
errz	377	905	6.9	28.2	6.8	16.3	100.0	73.6
errz_fpb	377	791	6.9	24.7	6.8	14.3	100.0	64.3
errz_other	0	114	0	3.6	0	2.1	0.0	9.3
errxy	0	123	0	3.8	0	2.2	0.0	10.0
num_identified	5481	3207	107.4	162.2	98.9	57.8		
total_num_outliers	377	1230	7.4	62.2	6.8	22.2		
num_measured	5104	1977	100	100	92.1	35.7		
true_num	5544	5544	108.6	280.4	100	100		

cmin: measured similarity < similarity threshold.
errz: measured z-error > z-error threshold.
errz_fpb: focal plane bias error.
errz_other: measured z-error > z-error threshold, but not focal plane bias error.
errxy: measured in-plane error > in-plane error threshold.
num_identified: total number of identified particles.
total_num_outliers: total number of measurements discarded as outliers.
num_measured: total number of valid measurements.
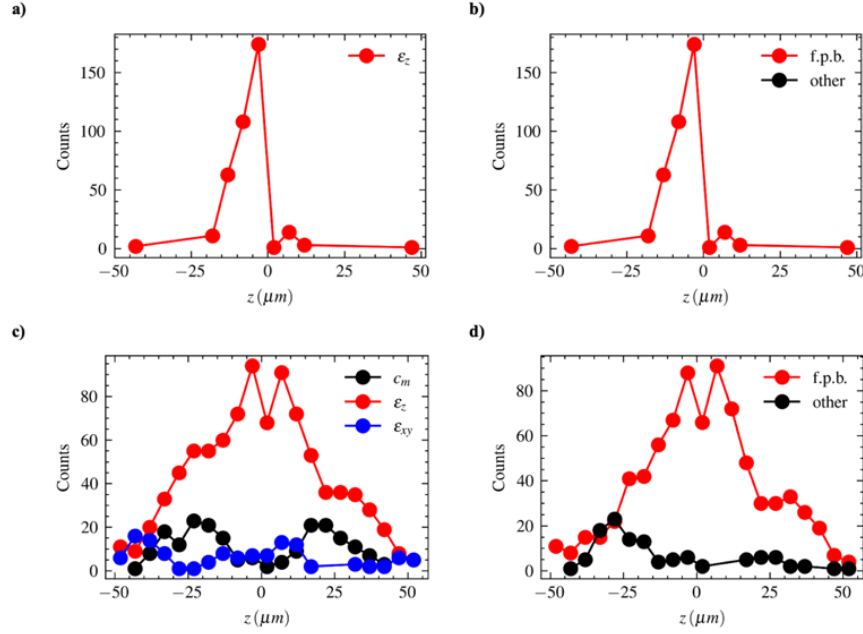true_num: total number of measurable particles.

Figure S7. Outliers by type and depth position for IDPT and GDPT. (a) The number of IDPT outliers by type and by depth position. Note: all IDPT outliers were due to depth measurement errors, so no other categories are plotted. (b) The number of IDPT depth measurement outliers due to focal plane bias errors (red) and non-focal plane bias others (black, "other"). Note: all IDPT depth measurement outliers were focal plane bias errors, so no data is shown for "other". (c) The number of GDPT outliers by type and by axial position. (d) The number of GDPT axial error outliers due to focal plane bias errors (red) and non-focal plane bias others (black, "other"). Counts (circles) are only shown for depth positions where counts ≥ 1. Line plots are included as a visual guide.

Note S8. Particle-to-particle similarity
We define the widefield similarity S_{wf} as the average similarity between all non-overlapping particle images in a single frame,

$$S_{wf} = \langle S(I_i, I_j) \rangle$$

where i and j are any two particle image templates for all i, j combinations. A value of $S_{wf} = 1$ corresponds to perfect positive correlation between all evaluated particle images. S_{wf} quantifies the mean similarity between particle images at approximately the same depth position (z) but different lateral positions (x, y). Practically, the widefield similarity quantifies the similarity (dissimilarity) between particle images.

We imaged 2 μm diameter fluorescent particles on a polymer-coated glass slide in 1 μm increments from $z = -50$ to 55 μm (see figure 2) and evaluated S_{wf} at each depth position (figure S8). To evaluate only non-overlapping particle images, we identified candidate particles in each frame using an intensity threshold and then manually culled overlapping or false positive particles. Across the full axial range, the depth-averaged widefield similarity $\overline{S_{wf}}$ was 0.92.
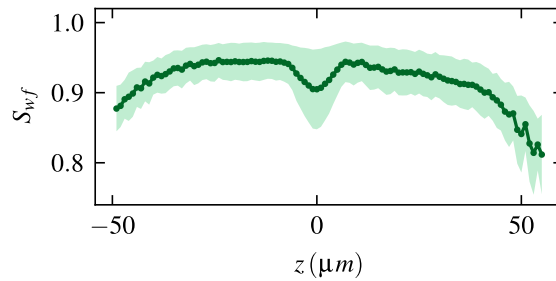

Figure S8. Widefield similarity S_{wf} (green points) with confidence intervals of ± 1 standard deviation (green shaded region) at each depth position z.

Note S9. Asymmetric similarity bias of IDPT

For optical systems that produce defocusing patterns that are nearly symmetric about the focal plane, cross-correlation between a target particle image against its calibration stack results in a similarity profile with two local maxima—each occurring approximately the same distance from focus but in opposite directions relative to the focal plane (i.e., $+z$ and $-z$). We show an example similarity profile in figure S9A, corresponding to the same particle as $I_c^{k=1}(z)$ in figure 2(b-d), where the local maximum similarity in the upper half axial range, $c_m(z > 0) = 0.988$, is slightly larger than the local maximum in the lower half axial range, $c_m(z < 0) = 0.972$. The difference between the two local maxima depends on the asymmetry of particle image defocusing, among other factors.
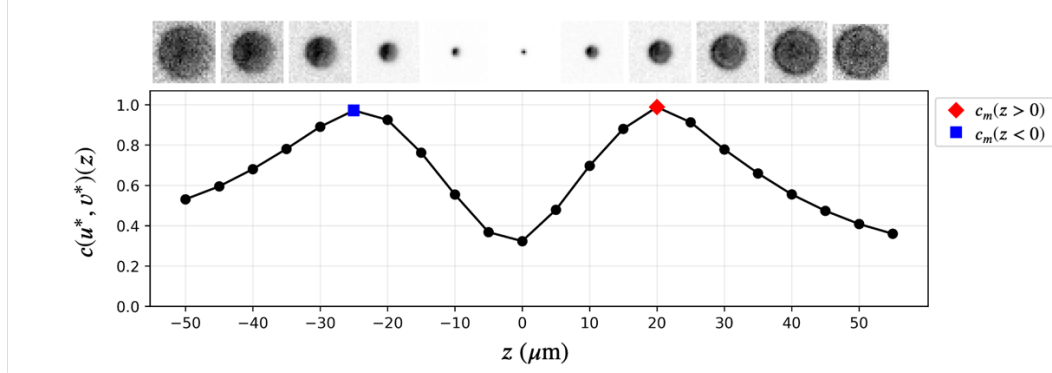

Figure S9A. Example similarity profile showing the maximum similarity between a target particle sub-image and each sub-image in a calibration stack, $c(u^*, v^*)(z)$. In this case, the global maximum similarity, $c_m = c(u^*, v^*, z^*)$, occurs approximately at the target particle's true depth position, $z^* = z \cong 20$ μm. The particle's sub-images are shown at depth positions $z = $ -50, -40, …, 40, and 50 μm, for reference.

To quantify the degree of measurable particle image asymmetry in our experimental images, we evaluate the ratio of the two local maximum similarity values. We define the asymmetric similarity c_{asym} as the ratio of the larger local maximum similarity divided by the smaller local maximum similarity. In this manner, $c_{asym} \cong 1$ corresponds to particle images with little focal plane asymmetry and c_{asym} values increasingly greater than one correspond to increasingly asymmetric particle images. Practically, c_{asym} values closer to one are indicative of measurements that are more likely to result in focal plane bias errors. For the example data shown in figure S9A, $c_{asym} = 0.988 / 0.972 = 1.017$. In figure S9B(a), we plot the depth positions measured by IDPT z_i' against the known positions z. We compare this to the local mean asymmetric similarity $\bar{c}_{asym}(z)$ at each depth position (figure S9B(b)) and show how smaller $\bar{c}_{asym}(z)$ values correspond to more frequent focal plane bias errors (figure S9B(c)). We attribute this to slight shift in the field of view between our calibration and evaluation images, measuring 2 pixels in the X-direction and 6 pixels in the Y-direction.
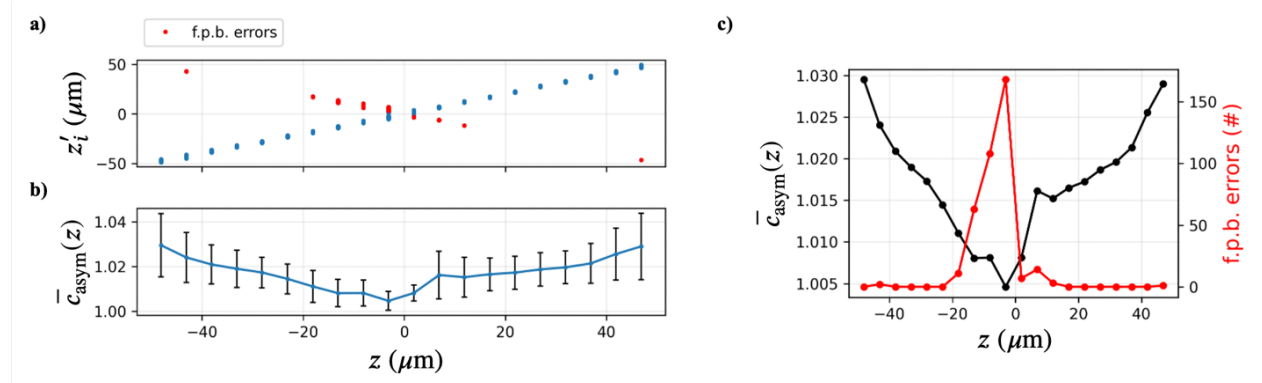

Figure S9B. (a) Depth positions measured by IDPT z_i' at each nominal depth position z. Depth positions that were deemed valid are shown as blue dots; focal plane bias errors are shown as red dots. (b) Mean asymmetric similarity $\bar{c}_{asym}(z)$ at each depth position z. Error bars correspond to two standard deviations. (c) Plot showing the asymmetric similarity $\bar{c}_{asym}(z)$ (black) and number of focal plane bias errors (red) as a function of depth position z. The number of focal plane bias errors is shown for all depth positions, including when equal to zero.

Note S10. Effect of sub-pixel position on axial errors

To evaluate the effect of sub-pixel position on axial measurement errors, we generated synthetic images of single particles at specified, sub-pixel lateral positions and 3D localized the particles using IDPT. The synthetic particle images were generated using MicroSIG [1] using the settings at the end of this note. Briefly, synthetic images were generated for a 2.15 μm diameter particle imaged using a 10X, 0.3NA objective lens and CCD sensor consisting of a 75x75 array of 16 μm pixels. The mean background intensity was 100 (arbitrary units). The noise level σ_I was 0 for the calibration images and 15 for the test images. The test images contain a single particle positioned at specified lateral displacements, Δx and Δy, relative to the calibration particle. We define Δr as the magnitude of the Δx and Δy displacements between the calibration particle I_0^c and the test particle $I_t^{i=0}$ (figure S10A(a)). The calibration images contain a single particle positioned at an in-plane position of $(x, y) = (37.5, 37.5)$ pixels (figure S10A(a-b)). We note that positions of 0.5 pixels correspond to the pixel center and positions of 0.0 or 1.0 correspond to the pixel edges. The calibration images spanned an arbitrary axial scale from -50 to +15 μm in 1 μm axial increments ($N_{cal} = 66$). We determined the focal position z_f to be positioned at $z = -4$ μm. To evaluate the influence of sub-pixel displacement and depth position on measurement performance, we generated 500 test images ($N_{test} = 500$) at regular axial intervals from -50 to +15 μm for each Δr displacement. Figure S10A(c) shows a single test particle positioned at an axial position of $z = -45$ μm and an in-plane position of $(x, y) = (38, 38)$ pixels, corresponding to $\Delta r = 0.707$ pixels. The defocused particle images have a bright outer edge below the focal position and blurred, Gaussian-like shape above. This is because the synthetic particle images generated by MicroSIG include optical effects due to spherical aberrations.
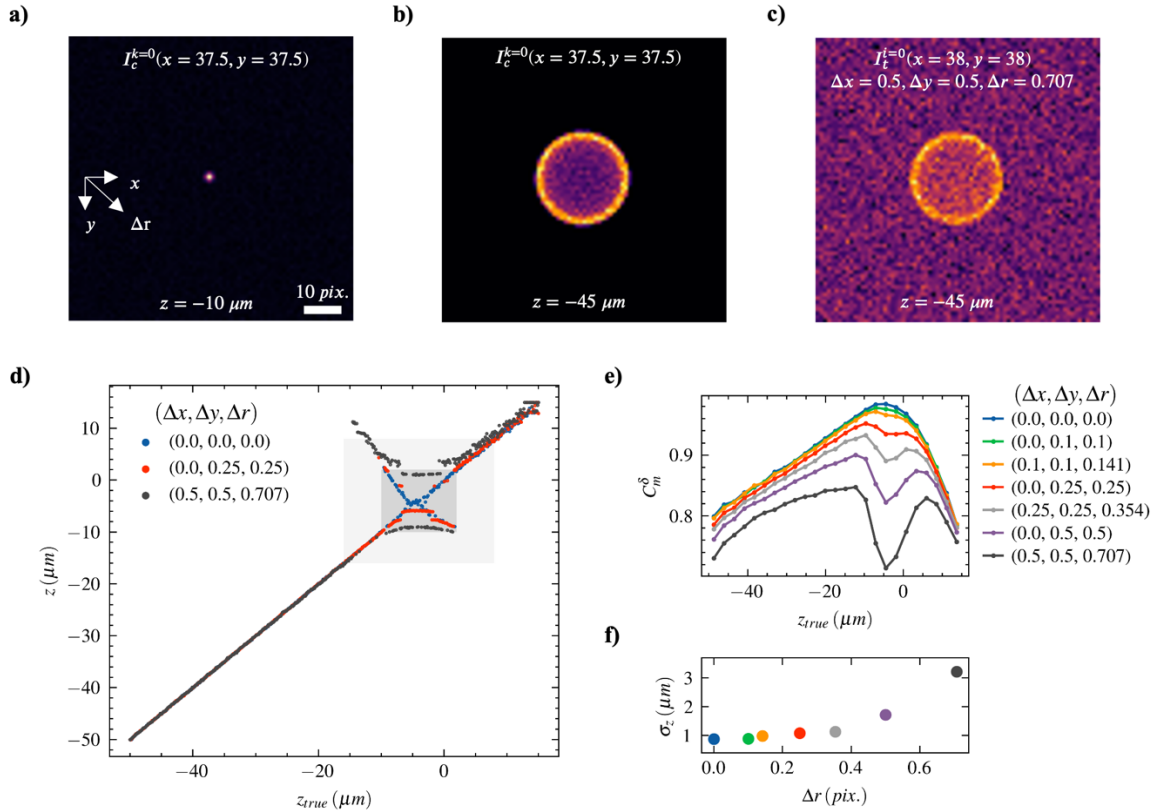

Figure S10A. (a) Synthetic calibration particle at an axial position of $z = -10$ μm. (b) Synthetic calibration particle at an axial position of $z = -45$ μm. (c) Synthetic test particle image with an in-plane position $(x, y) = (38, 38)$ pixels and axial position $z = -45$ μm, corresponding to $\Delta r = 0.707$ pixels. (d) Plot of measured axial position z as a function of true axial position z_{true} for Δr of 0 (blue), 0.25 (red), and 0.707 (black) pixels. Axial ranges defined by the depth of field and 2X the depth of field are shown as dark gray and light gray boxes, respectively. (e) Plot of local correlation coefficient c_m^δ as a function of true axial position z_{true} and sub-pixel displacement Δr. (f) Plot of the mean axial uncertainty σ_z as a function of sub-pixel displacement Δr. Colors corresponding to Δr are maintained across d-f for visual comparison.

We processed the images using IDPT to 3D localize the single particle in each frame. Figure S10A(d) shows the measured axial position z as a function of the true axial position z_{true} for $\Delta r = 0$ (blue), 0.25 (red), and 0.707 (black) pixels. Three phenomena are apparent: (1) focal plane bias errors occur near the depth of field, independent of Δr, (2) increasing Δr results in an increasing axial dead zone $\Delta z_{deadzone}$, where no particles are localized, and (3) axial localization accuracy is dependent on Δr and asymmetric relative to z_f.

First, although random noise is nearly negligible compared to the peak signal intensity ($\sigma_I \ll I_o$), the resulting deviations are evidently comparable to the depth dependent image information for particles located within the depth of field. This is demonstrated by the occurrence of focal plane bias errors for $\Delta r = 0$ (figure S10A(d): blue). The dependence of focal plane bias errors on the depth of field occurs because the focused particle images are sampled by a relatively small number of pixels and therefore contain relatively less low frequency information [2]. Additionally, the particle images change little through focus which decreases axial localization sensitivity. As the sub-pixel displacements become larger, focal plane bias errors occur across a wider axial range. For $\Delta r = 0.707$ pixels, this range extends to nearly 2X the depth of field. Second, we observe an axial dead zone $\Delta z_{deadzone}$, where no particles are localized, that expands as Δr increases. This dead zone stretches across an axial range of nearly 10 μm for $\Delta r = 0.707$ pixels. This likely results from a sub-pixel-dependent defocusing effect whereby particle positions on a pixel edge or corner cause the intensity distribution to spread out over a larger pixel area. This could result in particle images that appear slightly defocused relative to a particle image centered on a pixel. This is partly evidenced by the local correlation coefficients c_m^δ dependence on Δr (figure S10A(e)). Particularly near focus, increasing Δr results in significantly lower c_m^δ, although this dependence extends across the full axial range. Interestingly, lower correlation coefficients do not translate to increased axial localization errors for z less than 2X the depth of field (figure S10A(d): light gray box). However, for z greater than the depth of field, the axial localization accuracy is dependent on Δr. This asymmetry suggests that sub-pixel position dependence on axial localization is dependent on the particle image's intensity distribution, in addition to its size as discussed earlier. For z_{true} greater than the depth of field (figure S10A(d): dark gray box), the localized particle positions z are greater than z_{true} and proportional to Δr. This finding reiterates the sub-pixel-dependent defocusing effect described earlier. Finally, we observe the mean axial localization uncertainty σ_z is monotonically proportional to Δr (figure S10A(f)). Specifically, σ_z increases exponentially with Δr and is more than 3X higher for $\Delta r = 0.707$ pixels compared to $\Delta r = 0$ pixels (figure S10A(f)). This analysis highlights the importance of sub-pixel effects on image cross-correlation, as noted by [3].

Additionally, we briefly investigated the Δr dependence on the axial dead zone $\Delta z_{deadzone}$. We plot the measured axial position z as a function of true axial position z_{true}, for each Δr and z_{true} within ~2X the depth of field (figure S10B(a-g)). The axial dead zone $\Delta z_{deadzone}$, defined by the axial distance between the maximum z value for $z < z_f$ and the minimum z value for $z > z_f$, increases nearly quadratically with Δr (figure S10B(h)). Furthermore, the measured axial positions z are not symmetric along z_{true}, relative to z_f. This suggests sub-pixel position causes a sub-pixel-dependent defocusing bias.
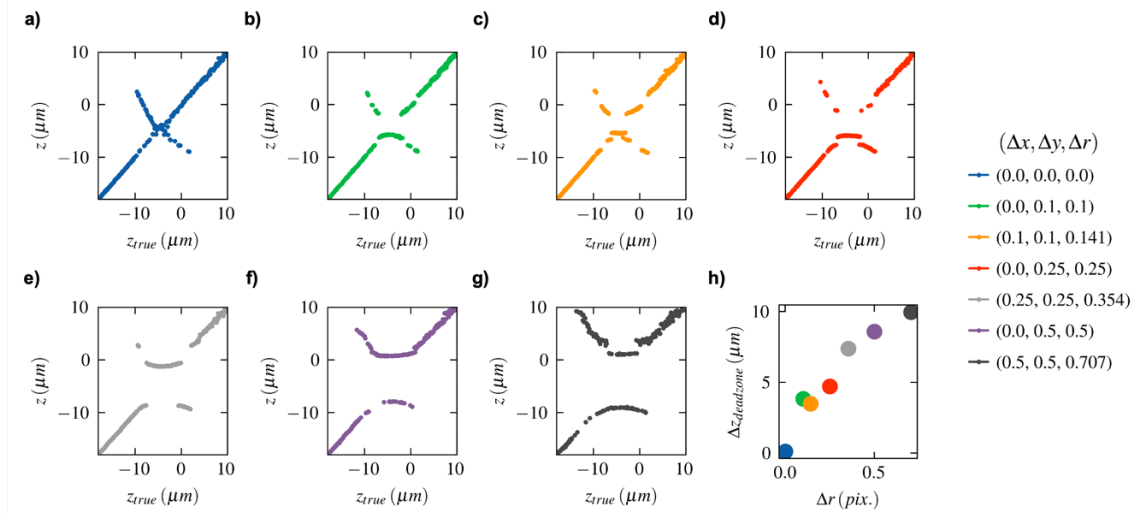

Figure S10B. (a-g) Plots of measured axial position z as a function of true axial position z_{true} for each Δr. (h) Plot of axial dead zone $\Delta z_{deadzone}$ as a function of sub-pixel displacement Δr. Colors corresponding to Δr are maintained across a-h for visual comparison.

Synthetic particle image generator settings:

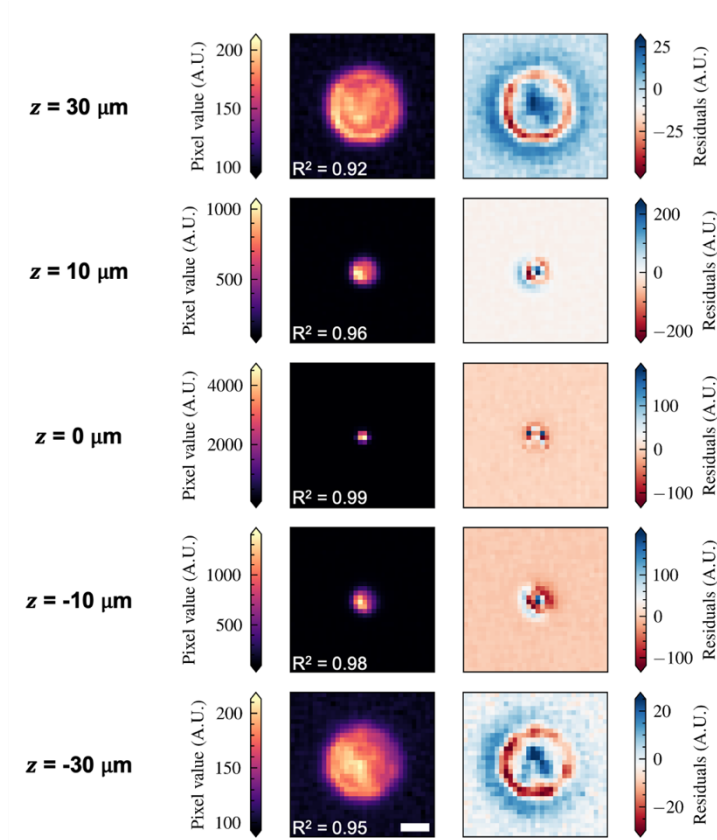|	
magnification:	10
numerical_aperture:	0.3
focal_length:	75
ri_medium:	1
ri_lens:	1.5
pixel_size:	16
pixel_dim_x:	75
pixel_dim_y:	75
background_mean:	100
points_per_pixel:	20
n_rays:	500
gain:	1
cyl_focal_length:	0
particle_diameter:	2.15
noise_level:	0 (calibration images), 15 (evaluation images)

Figure S11A. Particle images near image center and Gaussian fits. Particle images and 2D Gaussian fits for the particle corresponding to $I_c^{k=1}(z)$ in figure 2(b-d). The particle's in-plane distance from the image center r was 45 μm. Optical micrographs (false color) showing the particle image's sampled intensity distribution at z positions of -30, -10, 0, 10, and 30 μm. The coefficient of determination, R^2, values are shown in the bottom left corner of each image (left column). Residuals of fitting 2D Gaussian models to the particle images using the Levenberg-Marquardt algorithm (right column). Scale bar is 10 μm.
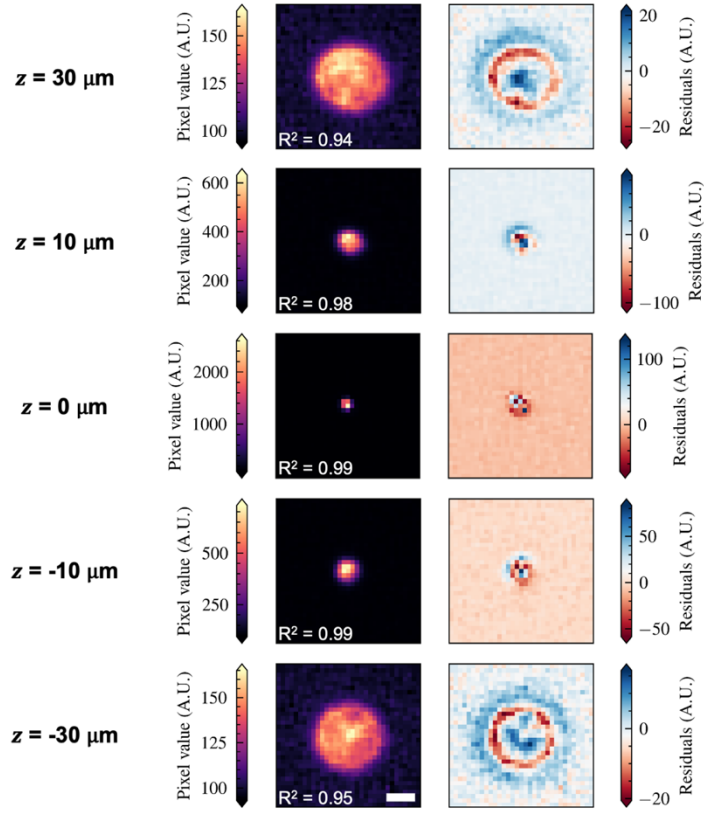
Figure S11B. Particle images near image edge and Gaussian fits. Particle images and 2D Gaussian fits for the particle corresponding to $I_c^{k=3}(z)$ in figure 2(b-d). The particle's in-plane distance from the image center r was 480 μm. Optical micrographs (false color) showing the particle image's sampled intensity distribution at z positions of -30, -10, 0, 10, and 30 μm. The coefficient of determination, R^2, values are shown in the bottom left corner of each image (left column). Residuals of fitting 2D Gaussian models to the particle images using the Levenberg-Marquardt algorithm (right column). Scale bar is 10 μm.

Table S12. IDPT measurement performance by calibration and target particle sub-image size

L_c (pixels)	L_t (pixels)	$\overline{c_m}$	$\overline{N_p'}/N_p$	$\overline{\sigma_{xy}}$ (μm)	$\overline{\sigma_z}$ (μm)
37	31	0.95	0.92	0.7	0.41
43	31	0.95	0.88	1.0	0.41
43	37	0.96	0.92	0.7	0.38
49	37	0.96	0.89	0.9	0.38
49	43	0.96	0.90	0.7	0.37

L_c: size of calibration particle sub-image.
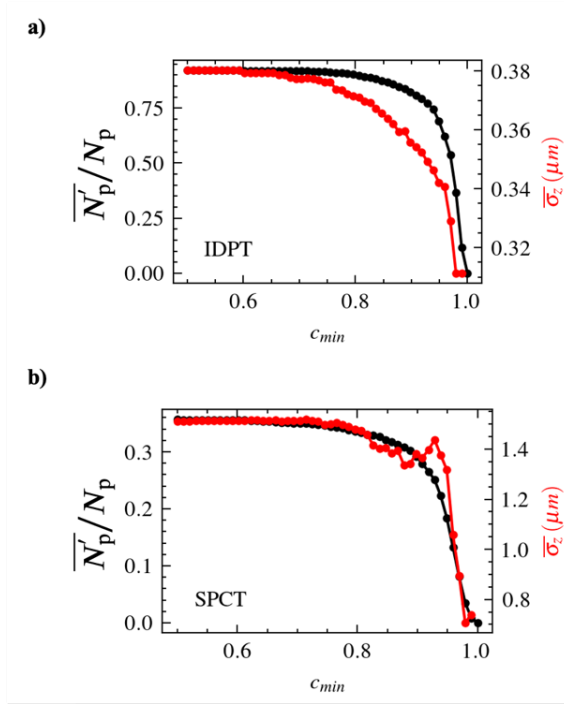L_t: size of target particle sub-image.

Figure S13. Depth-averaged axial uncertainty by similarity threshold. Global mean relative number of measured particles $\overline{N'_p/N_p}$ (black) and depth-averaged axial measurement uncertainty $\overline{\sigma}_z$ (red) for (a) IDPT and (b) GDPT as a function of similarity threshold c_{min}, where c_{min} is the minimum allowable similarity value such that measurements $c_m < c_{min}$ are discarded.
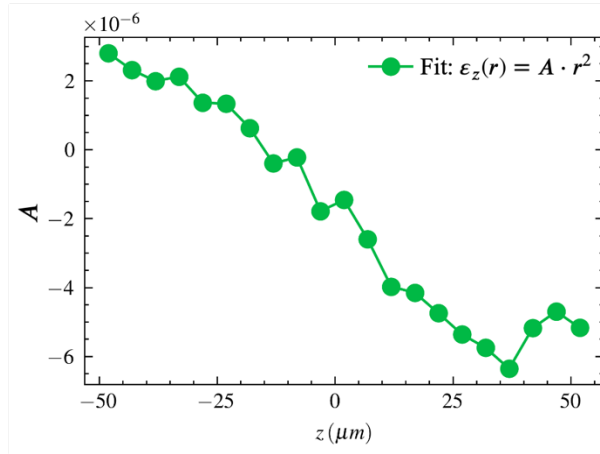

Figure S14. Apparent curvature variation with depth position for GDPT. The amplitude A of the parabolic functions, $\varepsilon_z(r) = A \cdot r^2$, fitted to GDPT's radially dependent depth measurement errors $\left(r'_i, \varepsilon_{z,i}\right)$ at each depth position z.
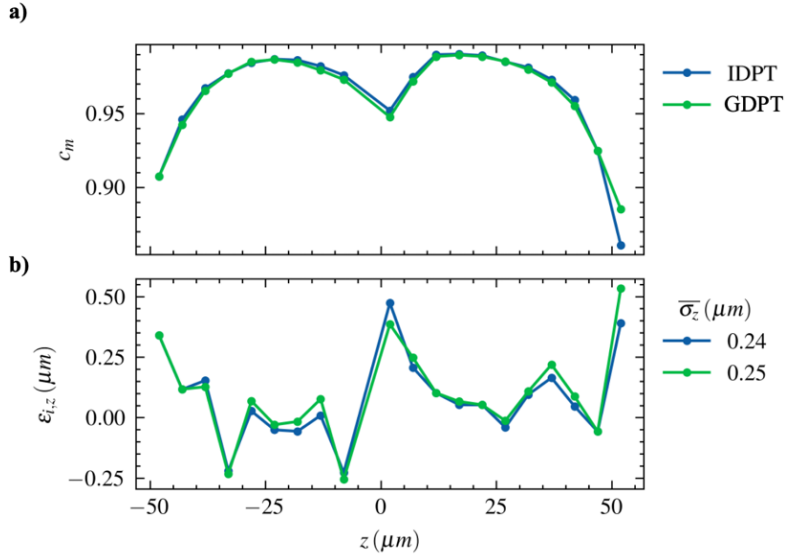
Figure S15. Comparison of IDPT and GDPT for single particle used for GDPT calibration. The (a) similarity c_m and (b) axial error $\varepsilon_{i,z}$ for IDPT (blue) and GDPT (green) for the particle used to generate GDPT's calibration model. The mean depth measurement uncertainty $\bar{\sigma}_z$ was 0.24 µm for IDPT and 0.25 µm for GDPT.

Note S16. DefocusTracker version 2.0.0 settings
DefocusTracker (referred to in the main work as GDPTlab) is an open-source 3D particle tracking software [4].

model:

Field	Value
type	"model"
method	"method_1"

model.training:

imwidth	38
imheight	38
gauss_filter	0
median_filter	0
boundary_threshold	10
smoothing	0
n_interp_images	0
imresize	1

model.processing:

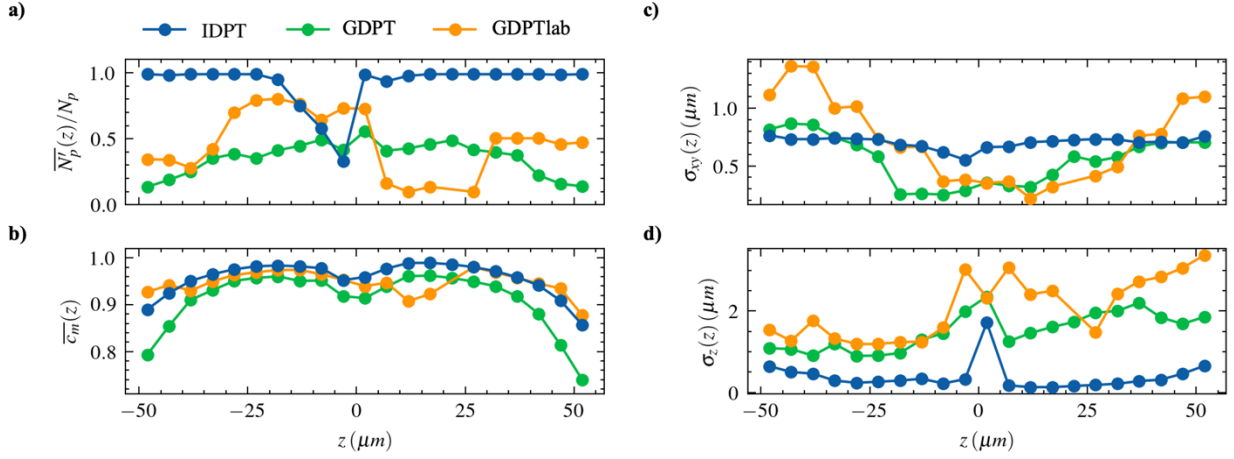| cm_final	0.7
cm_guess	0.4
no_overlap_radius	0.1
subimage_interpolation	1
walking_step	1
images_in_guess_step	9
n_iteration	2

Figure S17A. Comparison of IDPT, GDPT, and GDPTlab measurement performance. Comparison of depth-dependent measurement performance for IDPT (blue), GDPT (green), and GDPTlab (orange), showing (a) local mean relative number of measured particles $\overline{N_p'}(z)/N_p$, (b) local mean similarity $\overline{c_m}(z)$, (c) local mean in-plane uncertainty $\sigma_{xy}(z)$, and (d) local mean axial uncertainty $\sigma_z(z)$ evaluated at each depth position z.
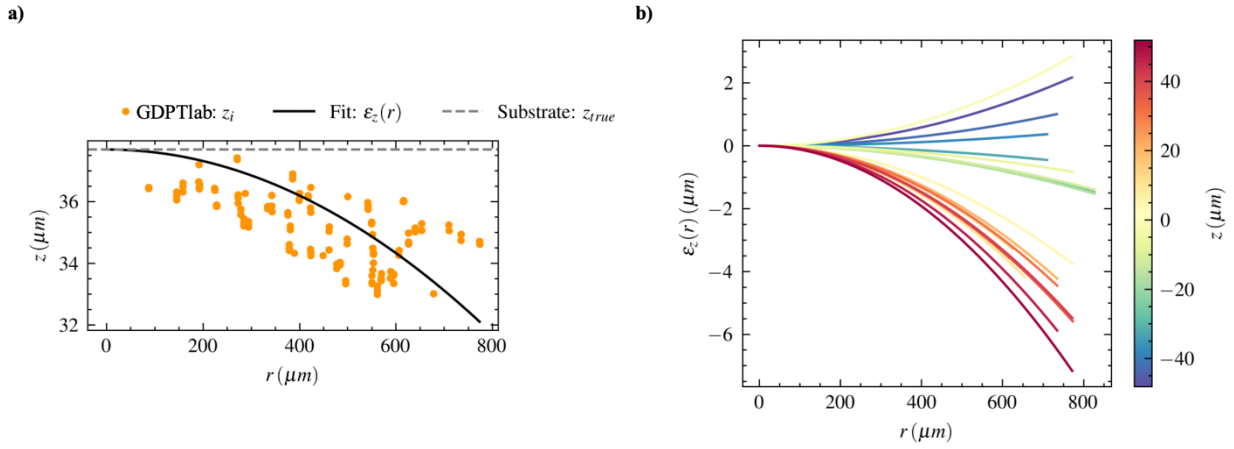

Figure S17B. Radial-dependence of depth measurement errors for GDPTlab. (a) Measured depth positions shown as a function of r for GDPTlab (orange dots) at $z = 37.7$ μm. GDPTlab's radially dependent z-errors $\left(r_i', \varepsilon_{z,i}\right)$ are visualized by fitting a parabolic function, $\varepsilon_z(r) = A \cdot r^2$ (black line), where A is sought by least-squares fitting. The true depth position z_{true} (gray dashed line) is shown for reference. (b) Parabolic functions $\varepsilon_z(r)$ fitted to $\left(r_i', \varepsilon_{z,i}\right)$ of GDPTlab at each depth position (see colorbar).
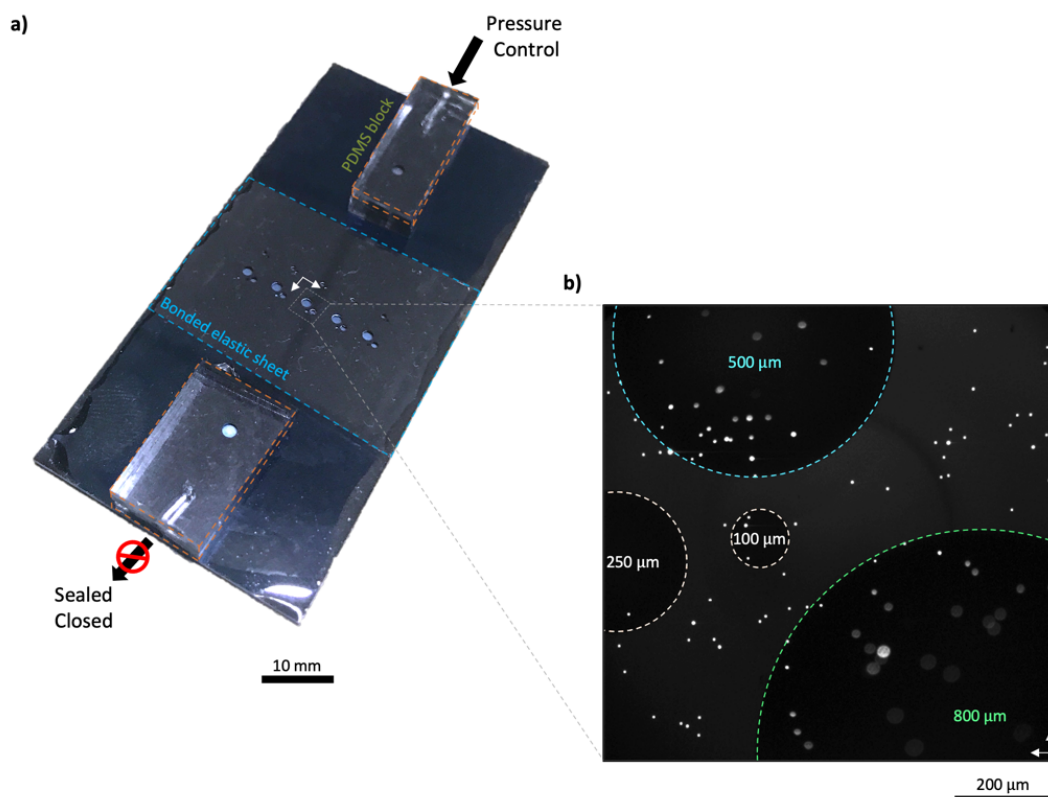
Figure S18. Experimental apparatus for dynamic surface profilometry. (a) Experimental apparatus comprising a sealed conduit with suspended elastic discs of varying radii. The conduit was pressurized by actuating a handheld syringe connected to the open inlet (Pressure Control) via rubber tubing. (b) Experimental image showing particle images when the experimental apparatus is pressurized. The elastic discs of radii a = 800 and 500 μm are outlined using green and cyan dashed lines, respectively, and were the focus of our discussion. The particle images on these discs are more or less defocused due to spherical deformation of the discs. The elastic discs of radii a = 250 and 100 μm (white dashed lines) were not analyzed because the number of particles on these discs was insufficient to adequately resolve the discs' deflection profiles. The white arrows in the bottom right corner of (b) are also shown in (a) to indicate the orientation of the experimental image relative to the experimental apparatus.

Note S19. Comparison of IDPT measurements with COMSOL Multiphysics simulations
Finite element method (FEM) was implemented using COMSOL Multiphysics 5.3. The device was simulated in a two-dimensional (2D) symmetric model using the Solid Mechanics module. The elastic membrane was modeled as hyperelastic material using the Neo-Hookean model with a density of 1080 kg/m³, Poisson's ratio 0.499, Young's modulus 500 kPa, and Lamé parameters $\mu = 678.6$ kPa and $\lambda = 1.0714$ MPa. We modeled displacement for a 1000-μm radius disc where 0-800 μm were freely suspended and acted upon by an applied pressure load. The remaining 200 μm radius was free to deform except for the bottom edge, which was modeled as a Rigid Boundary. The model consisted of approximately 15,000 elements and was solved using a stationary direct solver. Simulations with pressures of -600, -300, -100, 100, 300, and 600 Pa were solved using the auxiliary sweep option.

We evaluate the local radial displacements as a function of radial position for positive and negative peak deflections w_o captured in several representative frames. The representative frames were specifically chosen to span a wide range of experimentally observed disc deflections. In figure S.17, the radial displacements of each particle measured by IDPT (scatter points) in each of six representative frames are shown in addition to the numerical model predictions of the radial displacement at the top surface of the disc (dashed lines). For $w_o > 0$ (figure S.17a), we matched three representative frames to the numerical model for applied pressures of 100, 300, and 600 Pa, corresponding to predicted peak deflections of 65, 100, and 125 μm. The peak deflections according to the fitted analytical model presented in paper, $w_o = 66$, 99, and 130 μm, correspond to frames 185, 188, and 196. For $w_o < 0$ (figure S.17b), we matched three representative frames to the numerical model for applied pressures of -100, -300, and -600 Pa, corresponding to predicted peak deflections of -70, -105, and -130 μm. The peak deflections of the analytical model, $w_o = -74$, -97, and -126 μm, correspond to frames 161, 163, and 170. For both positive (figure S.17a) and negative (figure S.17b) peak deflections, the radial displacements measured by IDPT agree with the predictions from the numerical model. Importantly, the numerical model predicts significant radial displacements near the boundary region ($r \approx 800$ μm) that could not be captured in our analytical plate model.
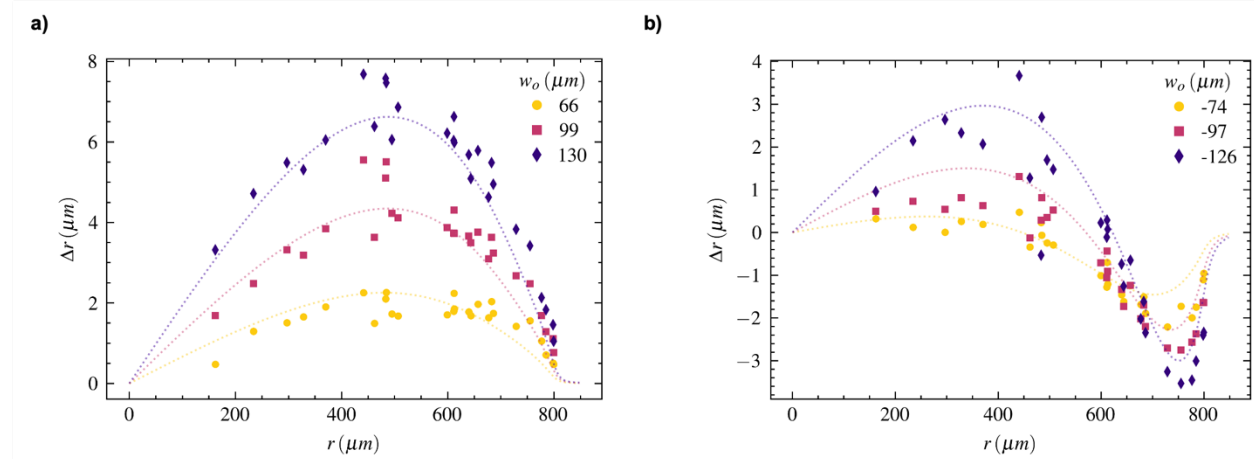

Figure S19. (a) For $w_o > 0$, we matched representative frames to the numerical model for applied pressures of 100, 300, and 600 Pa, corresponding to predicted peak deflections of 65, 100, and 125 μm. The peak deflections $w_o = 66$, 99, and 130 μm correspond to frames 185, 188, and 196. (b) For $w_o < 0$, we matched representative frames to the numerical model for applied pressures of -100, -300, and -600 Pa, corresponding to predicted peak deflections of -70, -105, and -130 μm. The peak deflections $w_o = -74$, -97, and -126 μm correspond to frames 161, 163, and 170.

Supplementary Movie Captions:

Movie S1. Animation of in-plane displacements. Fluorescent particles were randomly distributed onto the surface of an elastic sheet with suspended elastic discs of radii 800, 500, 250, and 100 μm. A series of 200 evaluation images were recorded while a handheld syringe was actuated, beginning after t = 1.64 s (40 images), to quasi-periodically inflate the discs, causing the particles to shift in-plane. We processed the images using IDPT to localize the particles in each frame (red circles) and track their in-plane displacements over time (black arrows). The simultaneous 3D measurement of elastic discs of varying radii enables characterization of deflection-dependent and aspect-ratio-dependent deformation behavior and edge effects.

Movie S2. Animation of 3D surface reconstruction. An elastic sheet was bonded to an etched silicon substrate for form suspended elastic discs, of radii 800, 500, 250, and 100 μm, and a conduit that could be pressurized. The surface of the sheet was decorated with fluorescent particles and series of 200 evaluation images were recorded while a handheld syringe was used to apply a quasi-periodic pressure load, beginning after t = 1.64 s (40 images). We processed the images using IDPT to 3D localize the particles (black dots) and fit plate bending models to each disc in each frame, totaling more than 20,000 measurements of 104 particles, and spanning an axial range of 251 μm. We reconstruct the surface topography by assuming radial symmetry and extrapolating the fitted plate bending models beyond the field of view (gray box). The 800, 500, 250, and 100 μm radii discs are shown as blue, green, purple, and orange surfaces, respectively. The 250 and 100 μm radii discs are shown flat because the number of particles riding the discs was insufficient for surface reconstruction.

References:

1. Rossi M. Synthetic image generator for defocusing and astigmatic PIV/PTV. Meas Sci Technol. 2020 Jan 1;31(1):017003.

2. Lewis JP. Fast Normalized Cross-Correlation. Industrial Light & Magic; 1995. Available from: http://scribblethink.org/Work/nvisionInterface/nip.pdf

3. Barnkob R, Rossi M. General defocusing particle tracking: fundamentals and uncertainty assessment. Exp Fluids. 2020 Apr;61(4):110.

4. Barnkob R, Rossi M. *DefocusTracker*: A Modular Toolbox for Defocusing-based, Single-Camera, 3D Particle Tracking. J Open Res Softw. 2021 Jul 23;9(1):22.